Topological Defects in a Living Nematic Ensnare Swimming Bacteria

Mikhail M. Genkin
Engineering Sciences and Applied Mathematics, Northwestern University, 2145 Sheridan Road, Evanston, Illinois 60202, USA

Andrey Sokolov
Materials Science Division, Argonne National Laboratory, Argonne, Illinois 60439, USA

Oleg D. Lavrentovich
Liquid Crystal Institute and Chemical Physics Interdisciplinary Program, Kent State University, Kent, Ohio 44242, USA

Igor S. Aranson
Department of Biomedical Engineering, Pennsylvania State University, University Park, Pennsylvania 16802, USA
Materials Science Division, Argonne National Laboratory, Argonne, Illinois 60439, USA

(Received 17 November 2016; revised manuscript received 23 January 2017; published 8 March 2017)

Active matter exemplified by suspensions of motile bacteria or synthetic self-propelled particles exhibits a remarkable propensity to self-organization and collective motion. The local input of energy and simple particle interactions often lead to complex emergent behavior manifested by the formation of macroscopic vortices and coherent structures with long-range order. A realization of an active system has been conceived by combining swimming bacteria and a lyotropic liquid crystal. Here, by coupling the well-established and validated model of nematic liquid crystals with the bacterial dynamics, we develop a computational model describing intricate properties of such a living nematic. In faithful agreement with the experiment, the model reproduces the onset of periodic undulation of the director and consequent proliferation of topological defects with the increase in bacterial concentration. It yields a testable prediction on the accumulation of bacteria in the cores of $+1/2$ topological defects and depletion of bacteria in the cores of $-1/2$ defects. Our dedicated experiment on motile bacteria suspended in a freestanding liquid crystalline film fully confirms this prediction. Our findings suggest novel approaches for trapping and transport of bacteria and synthetic swimmers in anisotropic liquids and extend a scope of tools to control and manipulate microscopic objects in active matter.

DOI: 10.1103/PhysRevX.7.011029 Subject Areas: Biological Physics, Soft Matter

I. INTRODUCTION

Assemblages of interacting self-propelled particles transducing energy stored in the environment into mechanical motion are termed active matter [1]. Active matter reaches to both living and synthetic nonequilibrium systems, from macroscopic bird flocks and fish schools [2,3] to microscopic suspensions of microorganisms [4,5], cytoskeletal extracts [6–8], and self-phoretic colloids [9,10].

Suspensions of self-propelled particles such as swimming bacteria are among the simplest realizations of active matter. Experimental and theoretical studies revealed the onset of collective behavior and "bacterial turbulence" [4,5,11–14], reduction of the effective viscosity [15,16], and many other phenomena not present in equilibrium colloidal suspensions. Another important class of active matter is formed by nonmotile particles with apolar (or nematic) interaction, or "active nematics." The most known example of active nematic is a suspension of molecular motors and microtubules in the presence of "fuel" (adenosine-triphosphate) [17]. While individual particles (microtubules) are nonmotile, their pairwise interactions mediated by molecular motors result in the onset of "active stress" and relative microtubules sliding. Active nematics exhibit a complex spatiotemporal behavior [18] and even a long-range ordering of topological defects [19]. A theoretical understanding of active nematics was achieved by particle simulations [20], phenomenological hydrodynamic models [21,22], or by asymptotic reduction of the probabilistic Boltzmann equation for interacting particles to the Ginzburg-Landau-type model [23,24]. An equilibrium nematic liquid crystal (LC) model [25,26]

supplemented by a phenomenological active stress was used in a number of works [27–31]. These studies provided important insights into the annihilation dynamics of defects, velocity correlations, and the onset of "active turbulence." However, it is not clear to what extent the continuum models are connected to the experiment [17], and how model parameters are related to experimental conditions.

A biosynthetic active material represented by a suspension of motile bacteria in a nontoxic lyotropic nematic liquid crystal was conceived in Refs. [32–36]. The material exhibits unique optical and mechanical properties, including guidance of bacteria along the nematic director, visualization of nanometer-thick bacterial flagella [32], transport of cargo along bacterial trajectories [33], and dynamic self-assembly of bacterial clusters [35]. For higher concentrations of bacteria, a spontaneous onset of spatiotemporal director undulations, a proliferation of topological defects, and turbulentlike states were observed [32]. While this "living nematic" turbulence is reminiscent of that in the motor-microtubules system [17], the physical mechanisms governing the self-organization in these two active systems are very different. In contrast with the sliding microtubules system [17], there is no direct mechanical coupling between bacteria and liquid crystal molecules: swimming bacteria interact with a liquid crystal by hydrodynamic and elastic forces. Additionally, in the living nematic, the energy input is provided by swimming bacteria, whereas in the motor-microtubules system, it is due to relative sliding of nonmotile microtubules. Moreover, it is not clear to what extent the generic models of an active nematic [27–31] are applied to suspensions of self-propelled particles in a nematic fluid [32].

Here, we develop a predictive computational model describing a living nematic represented by bacteria swimming in a liquid crystal [32]. We take advantage of the fact that mathematical models for both constituents, suspending a lyotropic liquid crystal and the suspended bacteria in isotropic liquids, are well established and validated by experiments and simulations. Our model faithfully reproduces key experimental observations in [32] the undulation instability of the aligned nematic state with the increase in bacterial concentration leading to a proliferation of $\pm 1/2$ defects (disclinations) and the consequent onset of spatiotemporal chaos. The model also leads to a testable prediction on accumulation of bacteria in the cores of $+1/2$ defects and corresponding expulsion of bacteria from $-1/2$ defects. To verify this prediction, we conduct a dedicated experiment with a fluorescent strain of motile bacteria *Bacillus subtilis* suspended in a freestanding film of lyotropic liquid crystal disodium cromoglycate (DSCG). The experiment faithfully confirms our theoretical prediction. In addition to relevance to the physics of nonequilibrium systems, our findings suggest novel approaches for trapping and transport of bacteria and synthetic swimmers in anisotropic liquids.

II. MODEL

Our continuum model, linking the dynamics of a LC with the motility of bacteria, describes a large-scale collective behavior emerging in this active system. The model is motivated by experiments on suspensions of bacteria in liquid crystals in Ref. [32]. Since the experiments are performed in a thin-film geometry with the scale of the emergent patterns much larger than the cell thickness h [see Fig. 1(a)], we employ the depth-averaged quasi-two-dimensional description.

Our main assumptions are the following. (i) The volume fraction of bacteria is relatively low and does not perturb properties of the suspending liquid crystal. This assumption is justified by exceedingly small bacterial volume fractions (of the order of 0.2% or about 5×10^8 cells/cm^3) needed for the onset of instability [32]. The continuum description is justified as long as the emergent pattern wavelength (about 500 μm near the threshold) is large compared to the

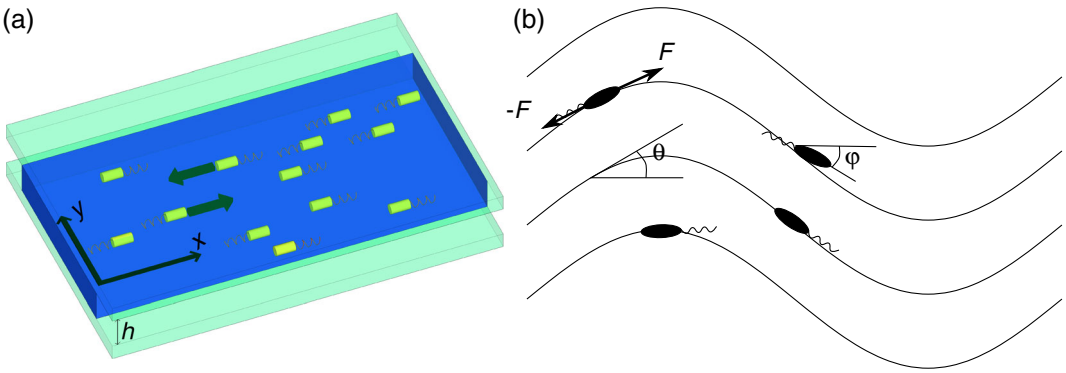

FIG. 1. Schematics of experimental cell. (a) A liquid crystal suspension of motile bacteria is sandwiched between two glass plates with the separation h [32]. A specific treatment of the glass plate inner surface anchors the LC director $\mathbf{n}$ along the x axis. Bacteria exhibit apolar interaction: bacteria swimming in the opposite direction can pass without collision. (b) Illustration of bacterial alignment along the LC director $\mathbf{n}$. Swimming bacteria impose a pair of forces $\pm\mathbf{F}$ (force dipole) on the LC.

interbacteria distance, ~10 μm. (ii) The suspended bacteria tend to align with the local nematic director $\mathbf{n} = [\cos(\theta), \sin(\theta)]$, where $-\pi/2 \leq \theta < \pi/2$ is the nematic angle; see Fig. 1(b). This assumption is justified by the fact that a rod-shaped object with a planar surface anchoring, such as a bacterium, tends to align with the local director $\mathbf{n}$. A misaligned configuration would cost higher elastic energy [37]. Our analysis indicates that the alignment of bacteria with the LC director happens on a time scale of 1 sec, which is smaller than any characteristic time of collective behavior. (iii) Interactions between bacteria are apolar; see Fig 1(a). This assumption is justified by our quasi-two-dimensional approximation: In a two-dimensional view, bacteria traveling in opposite directions can pass without collision at slightly different heights. Thus, we assume that at each point x, y we may have two concentrations of bacteria c^+ and c^-, swimming in opposite directions, $\mathbf{n}$ and $-\mathbf{n}$ (compare with Ref. [38]).

We employ the well-established Edwards-Beris model for LC in terms of a tensorial order parameter $\mathbf{Q}$ [26]:

$$(\partial_t + \mathbf{v}\cdot\nabla)\mathbf{Q} - \mathbf{S} - \Gamma\mathbf{H} + \mathbf{F}_{\text{exter}} = 0. \tag{1}$$

Here, $\mathbf{Q} = q(\mathbf{nn} - \mathbf{I}/2)$ is a traceless symmetric tensor, $\mathbf{n} = [\cos(\theta), \sin(\theta)]$ is a nematic director, $\mathbf{I}$ is the identity tensor, $q > 0$ is the magnitude of the order parameter, Γ is a director relaxation rate, $\mathbf{H}$ is a molecular field, $\mathbf{v}$ is a flow velocity, and $\mathbf{S}$ is a tensor containing the velocity gradients and $\mathbf{Q}$. Expressions for $\mathbf{H}$ and $\mathbf{S}$ are given in the Appendix. The last term in Eq. (1) describes the aligning effect of the external field $\mathbf{F}_{\text{exter}}$, which arises in our case due to surface anchoring.

The linear momentum balance equation is of the form

$$\nabla\cdot(\boldsymbol{\sigma}_a + \boldsymbol{\sigma}_s + \boldsymbol{\sigma}_{\text{act}} + \boldsymbol{\sigma}_{\text{visc}} - p\mathbf{I}) - \zeta\mathbf{v} = 0. \tag{2}$$

Here, $\boldsymbol{\sigma}_a$, $\boldsymbol{\sigma}_s$, $\boldsymbol{\sigma}_{\text{visc}}$ are, correspondingly, symmetric, antisymmetric, and viscous contributions to the stress tensor (see the Appendix and the Supplemental Material [39]). Fluid is assumed to be incompressible, and the hydrodynamic pressure p can be eliminated by the incompressibility condition $\nabla\cdot\mathbf{v} = 0$. The viscous friction term $-\zeta\mathbf{v}$ originates from depth averaging of the flow profile, $\zeta = 12\eta/h^2$, where η is the isotropic viscosity (compare Refs. [14,29]).

A self-propelled particle, such as a motile bacterium, exerts a pair of forces on the suspending fluid (force dipole or stresslet); see Fig. 1(b) [40]. In the continuum description, the distribution of force dipoles results in an active stress $\boldsymbol{\sigma}_{\text{act}}$. In a dilute limit, the active stress $\boldsymbol{\sigma}_{\text{act}}$ can be written as [13,41]

$$\boldsymbol{\sigma}_{\text{act}} = -\Lambda c\left(\mathbf{pp} - \frac{\mathbf{I}}{2}\right), \tag{3}$$

where $\Lambda > 0$ is the magnitude of the force dipole imposed by a swimmer [the minus sign in front of Eq. (3) corresponds to pusher swimmers such as bacteria], c is the concentration of bacteria, and $\mathbf{p} = [\cos(\phi), \sin(\phi)]$ is the unit vector in the propulsion direction. We assume that the local orientation angle of bacteria ϕ is governed by the following relaxation equation:

$$\partial_t\phi = \frac{1}{\tau_0}\sin(2\theta - 2\phi) + D_r\nabla^2\phi. \tag{4}$$

The first term describes the relaxation of the bacterial orientation angle towards the nematic angle θ with the relaxation rate τ_0 (compare Ref. [37]). The last term describes the diffusion of orientation with the rotational diffusion D_r. We assume that elastic effects in the LC dominate flow alignment and neglect the advection and shear aligment terms, such as in Ref. [13].

The relaxation time τ_0 is determined by the balance of the orientation-stabilizing elastic torque and the viscous torque, $\Gamma_{\text{el}} + \Gamma_{\text{visc}} = 0$. A bacterium can be approximated by a long rod of length l and radius r. Assuming that the rod aligns the surrounding director parallel to its axis, the stabilizing elastic torque acting on the rod misaligned by an angle $\alpha = \phi - \theta$ is $\Gamma_{\text{el}} = 4\pi K l\alpha/\ln(2l/r)$, where K is the average value of the Frank elastic constant [42]. The viscous torque is approximated as $\Gamma_{\text{visc}} = \kappa\overline{\eta}\partial_t\alpha$, where $\kappa = \pi l^3/3[\ln(l/2r) - 1/2]$ is the geometrical friction factor for a prolate ellipsoid [43] of an aspect ratio close to that of a bacterium, $l/2r \approx 7$, and $\overline{\eta}$ is the effective drag viscosity that depends on the director orientation. Thus, the relaxation time is

$$\tau_0 \approx \frac{\overline{\eta}l^2}{12K}\frac{\ln(2l/r)}{\ln(l/2r) - 1/2}. \tag{5}$$

Neglecting the angular dependence of the viscosity $\overline{\eta}$, for typical experimental values for lyotropic chromonic liquid crystals [44], $\overline{\eta} = 4$–$5\ \text{kg m}^{-1}\ \text{sec}^{-1}$, $K = 15$ pN, and for $l = 5\ \mu$m, $r = 0.4\ \mu$m, one estimates $\tau_0 \approx 1$–1.5 sec.

Since the relaxation time τ_0 is small (of the order of 1 sec), bacteria rapidly align with the director $\mathbf{n}$. Thus, we set the vector $\mathbf{p}$ to be either parallel ($\phi = \theta$) or antiparallel ($\phi = \theta + \pi$) to the nematic orientation $\mathbf{n}$ replace $\mathbf{pp} \to \mathbf{nn}$ in Eq. (3). By solving Eq. (4), we verify that the main results are unchanged as long as τ_0 is small enough.

The transport of bacteria in LC is governed by two coupled advection-diffusion equations for the concentrations $c^{\pm}$ of bacteria swimming parallel (c^+) or antiparallel (c^-) to the director $\mathbf{n}$ (compare also with the approach in Refs. [38,45]):

$$\begin{aligned}
\partial_t c^+ + \nabla\cdot(V_0\mathbf{n}c^+ + \mathbf{v}c^+) &= -\frac{c^+ - c^-}{\tau} + D_c\nabla^2 c^+,\\
\partial_t c^- + \nabla\cdot(-V_0\mathbf{n}c^- + \mathbf{v}c^-) &= -\frac{c^- - c^+}{\tau} + D_c\nabla^2 c^-.
\end{aligned} \tag{6}$$

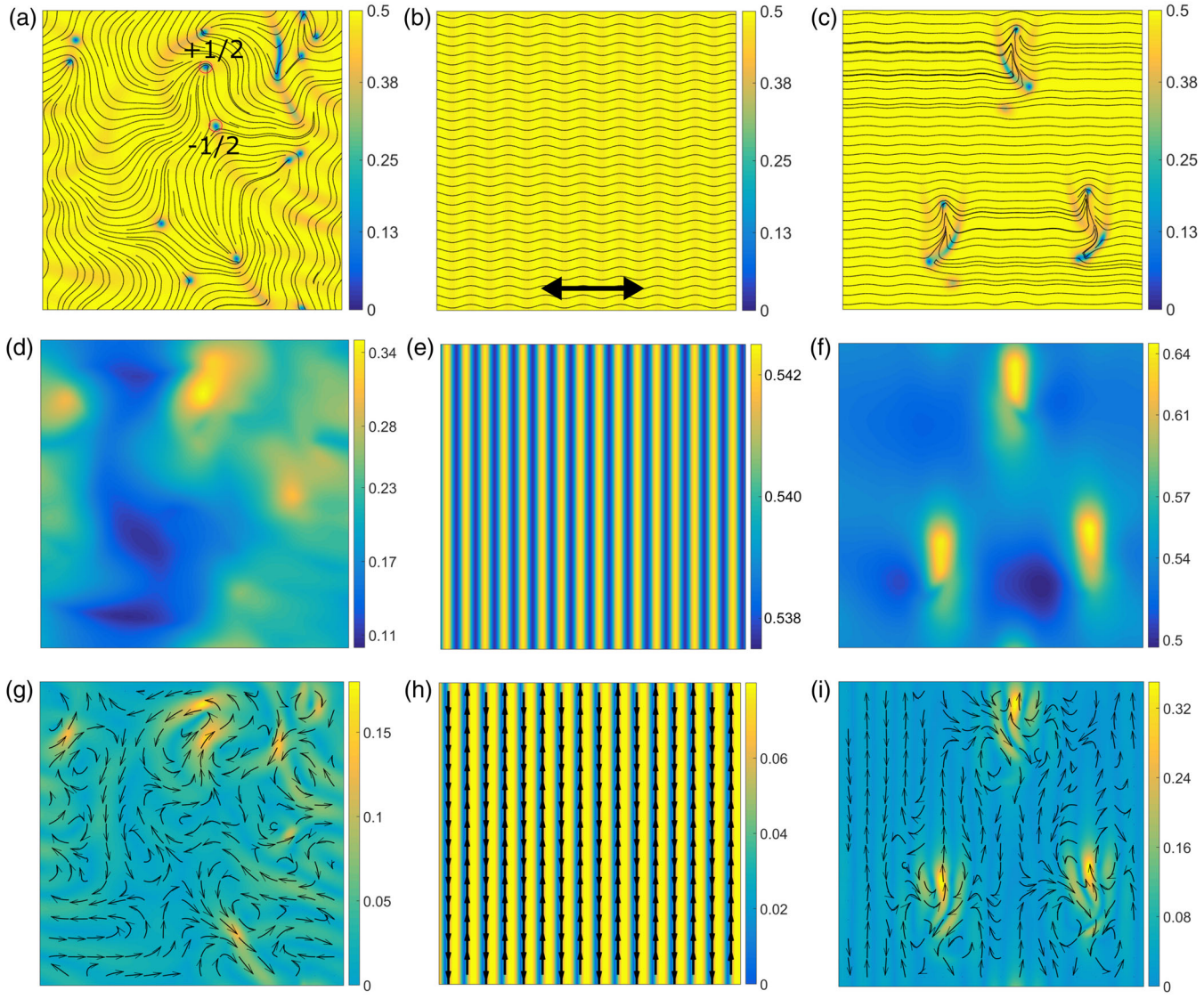

FIG. 2. Results of computational modeling. Nematic orientations and magnitudes of the order parameter (a)–(c), concentration fields (d)–(f), and flow velocity magnitudes with streamlines (g)–(i). Panels (a), (d), and (g) depict a state with defects for zero anchoring and average concentration $c_0 = 0.2$. Some $\pm 1/2$ topological defects are shown. Panels (b), (e), and (h) display stable periodic configuration with surface anchoring ($\xi_{an} = 0.05$) and $c_0 = 0.54$, i.e., near the instability threshold. The thick black arrow indicates the prescribed director orientation set by the surface anchoring. Panels (c), (f), and (i) illustrate hysteretic behavior: the configuration with defects exists for the same parameter values ($\xi_{an} = 0.05$, $c_0 = 0.54$) as in (b), (e), and (h). Other model parameters are $\tau = 66.6$, $D_c = 4$, Er $= 3.75$, $\Lambda = 1$, $\zeta = 0.2$, $\Gamma = 0.5$. See also Videos 1–4 in Supplemental Material [39].

Here, V_0 is the bacterium swimming speed, D_c is the diffusion coefficient, and τ is the direction reversal time (if a bacterium reverses a direction, it leaves the population c^+ and becomes c^-, or vise versa). Our experiments show that the reversal time is typically quite large, of the order of 30 sec. The reversals are related to bacterial run-and-tumble behavior. Since in liquid crystals the bacteria can move only along the director, tumbling is suppressed, and only back and forth movements are permitted. Since a low-tumbling strain of *B. subtilis* is used in our experiments, the reversal time τ is very large compared to the bacterial reorientation time τ_0.

We rewrite Eq. (6) for the total concentration $c = c^+ + c^-$ and the concentration difference (or polarization) $w = c^+ - c^-$:

$$\partial_t c + \nabla \cdot (V_0 \mathbf{n} w + \mathbf{v} c) = D_c \nabla^2 c,$$
$$\partial_t w + \nabla \cdot (V_0 \mathbf{n} c + \mathbf{v} w) = -\frac{2w}{\tau} + D_c \nabla^2 w. \qquad (7)$$

In the limit of very small reversal time, $\tau \to 0$, the polarization w becomes enslaved and one derives $w \approx V_0 \tau \nabla \mathbf{n} c/2$. Plugging it into the equation for c, we obtain the concentration evolution similar to that of active

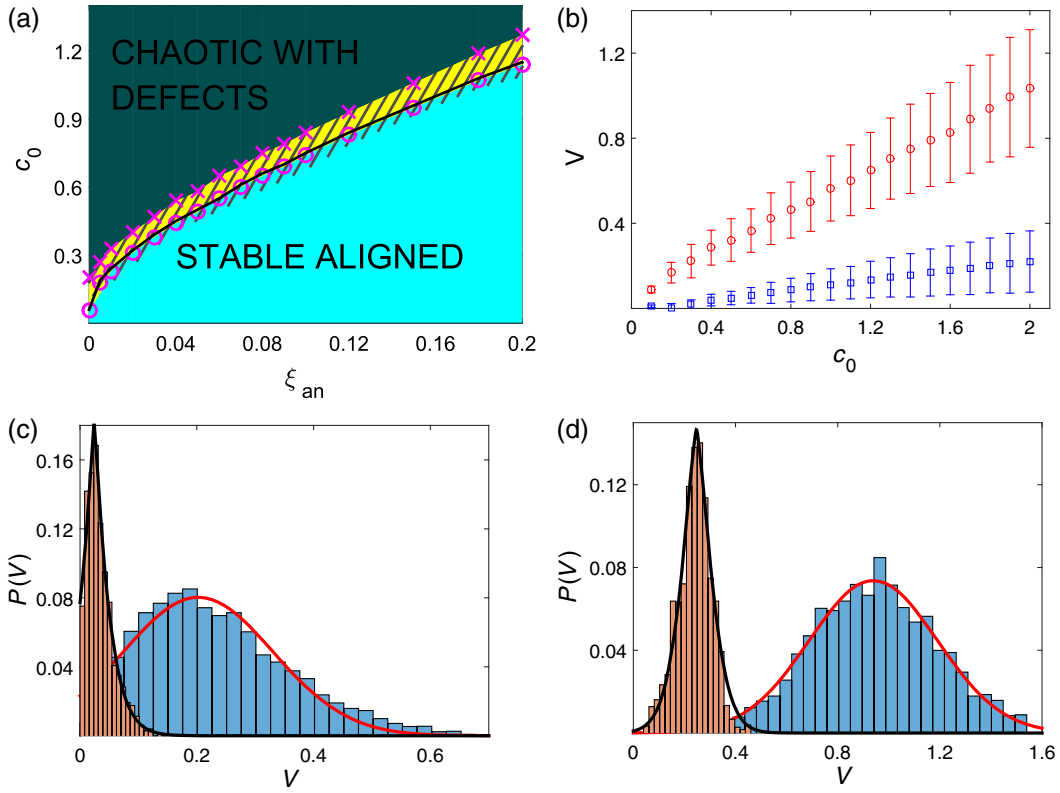

FIG. 3. Characterization of defect dynamics. (a) Phase diagram. Symbols circle, times depict the simulations results. The black solid line indicates the linear stability limit, Eq. (9). Stable director undulations exist between defect and homogeneous aligned states (yellow band). The transition boundaries are obtained by gradually increasing the average concentration c_0 from a slightly perturbed homogeneous initial condition. Hatching shows the hysteresis band where nonvanishing defects coexist with the undulated or homogeneous aligned states, $\tau = 66.6$ (corresponding, approximately 20–30 sec for the conditions of our experiment). (b) Mean velocity $\bar{V}$ of $+1/2$ defects (circle, red) and $-1/2$ defects (square, blue) vs c_0. Error bars are the velocity standard deviations. The velocity distributions for $-1/2$ (c) and $1/2$ defects (d) for $\xi_{an} = 0$ and for $c_0 = 1.8$ (blue) and $c_0 = 0.3$ (brown). Red solid lines are Gaussian fits and solid black lines are the stretched exponential fits.

nematics [27–31,46]. However, for the conditions of our experiment [32], this reduction is nonphysical.

III. RESULTS

A. Simulations results

Select results for different model parameters are presented in Fig. 2 and Videos 1–4 in Supplemental Material [39]. A complete description of the computational model and the implementation details are included in Supplemental Material [39]. For zero surface anchoring ($\xi_{an} = 0$), the system remains in a stable uniform state below the critical concentration c_{cr} [see also Fig. 3(a)]. Gradually increasing the concentration c above c_{cr} we observe first the onset of stable periodically undulated states followed by a spatiotemporal chaos characterized by motion, spontaneous nucleation or annihilation of topological defects, and flow generation in nematic; see Figs. 2(a), 2(d), and 2(g), similar to that observed in experiment [32]. This chaotic behavior is reminiscent of that observed in active nematics [27–31]. However, in contrast to the previous studies, we note a significant accumulation of bacteria in the cores of $1/2$ defects and expulsion of bacteria from the cores of $-1/2$ defects; see Fig. 2(d). We also observe that the transition to the spatiotemporal chaos is associated with a substantial hysteresis: uniformly aligned and stationary modulated states coexist with defects for the same value of the concentration near the threshold. The main reason for the hysteresis is the bacteria accumulation in the cores of positive defects, which, in turn, locally increases the activity of the system [active stress, Eq. (3), is proportional to the concentration].

Figures 2(b), 2(e), and 2(h) displays stable configurations characterized by periodic undulations of a nematic that was initially aligned along the prescribed direction. These undulations cause modulation of the bacterial concentration c. In addition, these steady-state nematic distributions generate a sustained periodic pattern of counterpropagating flows, Fig. 2(h). With the further increase in the concentration c, the periodic pattern becomes unstable and gives way to the state with moving topological defects, Figs. 2(c), 2(f), and 2(i). In contrast to the zero surface anchoring case, the defects predominantly move perpendicular to the overall nematic

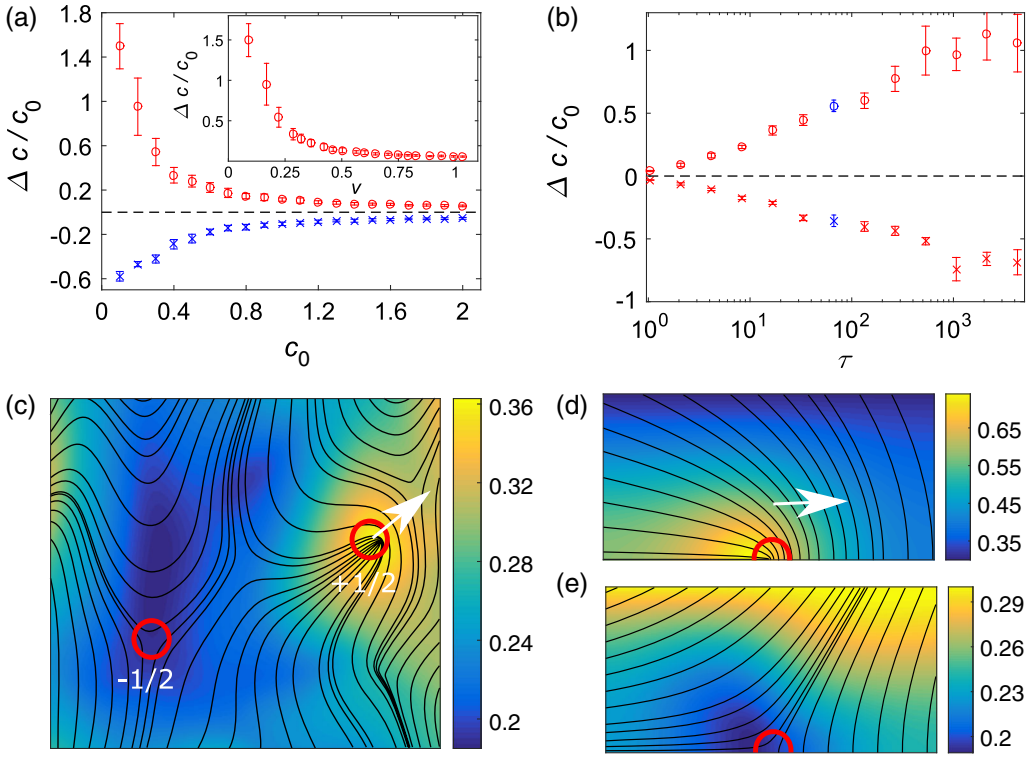

FIG. 4. Concentration distributions. Relative concentration difference $\Delta c/c_0$ vs c_0 for $\tau = 66.6$ (a) and vs τ for $c_0 = 0.3$ (b) for $1/2$ (circle) and $-1/2$ (times) defects. Inset: $\Delta c/c_0$ for $1/2$ defects vs defect velocity V. Blue symbols in (b) indicate $\tau = 66.6$ used in most of the simulations. Error bars are the standard deviations. (c) Close-up view of the concentration field c for $c_0 = 0.3$. Some defects are shown in red circles, white arrow indicates the direction of motion. Domain size is 40×40 units of length. Steady-state concentration distributions near $1/2$ defect (d) and $-1/2$ defect (e) obtained from Eq. (11) for $V = 0.5$. Size of the integration domain 40×20 units; due to reflection symmetry, only the upper half of the field c is shown.

direction (x axis in this case). This behavior is also consistent with the experiment on a confined suspension with surface anchoring [see Fig. 2(e) in Ref. [32]].

The phase diagram obtained by numerical integration of Eqs. (1), (2), and (7) in (c_0, ξ_{an}) space is shown in Fig. 3(a), where c_0 is the mean bacterial concentration. Numerical results are in excellent agreement with the theoretical expression for the instability threshold; see Eq. (9).

B. Statistics of topological defects

Figures 3 and 4 present a characterization of defects dynamics. The defect tracking algorithm is described in Supplemental Material [39]. Figure 3(b) shows mean defect velocities $\overline{V}$ vs the average concentration c_0. There is a velocity increase with the increase in concentration. The velocity of $1/2$ defects is higher than the velocity of $-1/2$ defects by a factor of 5. We find, in agreement with previous studies, Refs. [27,46], that an isolated $1/2$ defect moves persistently while the $-1/2$ defect is immobile. However, due to interactions, the $-1/2$ defects become entrained by the positive ones with the speed determined by their proximity. The speed of defects is practically independent of the anchoring strength ξ_{an}.

Velocity distributions of the defects $P(V)$ are shown in Figs. 3(c) and 3(d). We find that for high concentrations, the distributions $P(V)$ are well approximated by a Gaussian law $P(V) \sim \exp[-a_0(V - \overline{V})^2]$. In contrast, for lower c values, and correspondingly, for lower defect concentrations, the distributions are better approximated by a stretch exponential $P(V) \sim \exp[-a_1(V - \overline{V})^\zeta]$ with the exponent $\zeta \approx 1.13$ for $-1/2$ defects and $\zeta \approx 1.4$ for $1/2$ defects. We hypothesize that the defect motion is effectively randomized at high concentrations c (i.e., for high activity) leading to a Gaussian distribution. In contrast, for low concentrations, the defect dynamics is composed of long ballistic flights and rare nonelastic collisions. These kinds of processes often exhibit non-Gaussian statistics; see, e.g., Ref. [47].

Concentration distributions for moving defects are shown in Fig. 4. A close-up view of the concentration field for $\pm 1/2$ defects, Fig. 4(c), confirms accumulation behind the core of the $1/2$ defect and depletion for the $-1/2$ defect. The relative concentration difference $\Delta c/c_0$ decreases with the increase of the average concentration c_0, or, correspondingly, activity of the system, Fig. 4(a). Here, $\Delta c = c_{\max/\min} - c_0$, where the extrema of c are computed over the entire domain of

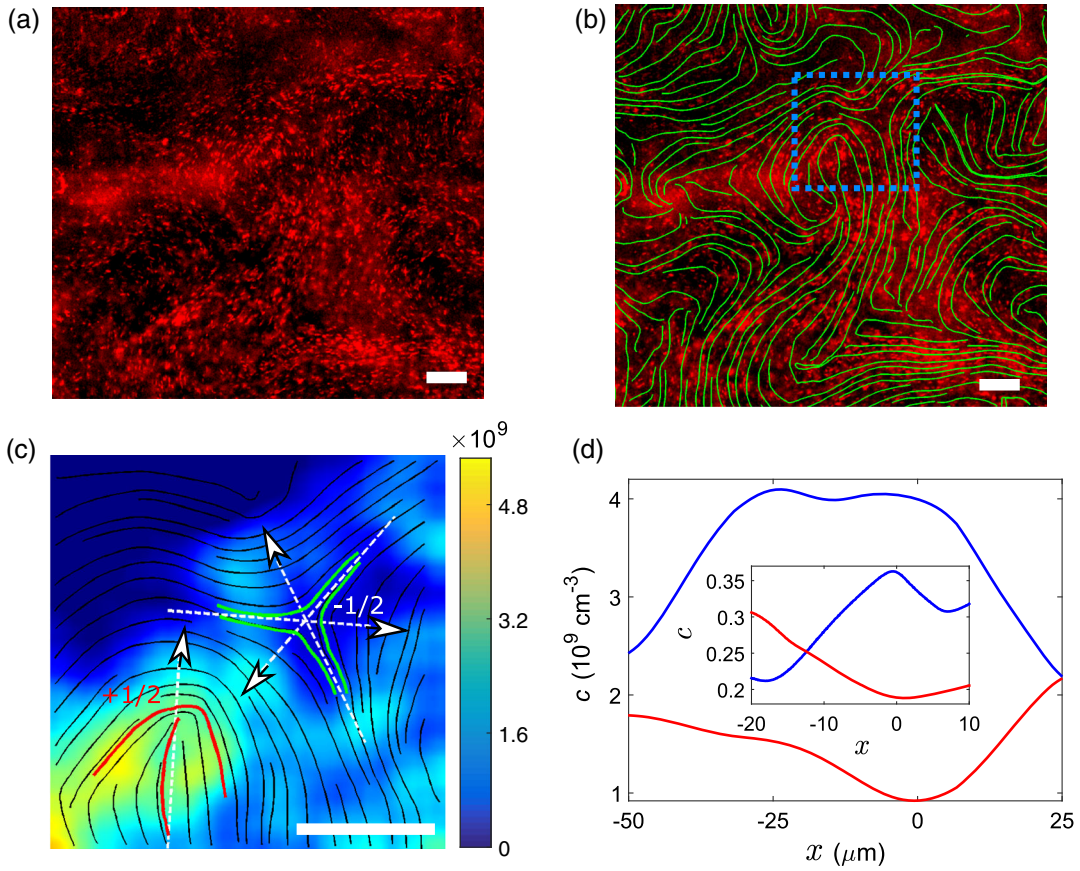

FIG. 5. Experimental verification. (a) Fluorescent image of swimming bacteria suspended in a freestanding LC film in the regime of chaotic motion. Average bacterial concentration $c \approx 2 \times 10^9$ cell/cm^3. Scale bar is 50 μm. See also Videos 5 and 8 in Supplemental Material [39]. (b) Digitally processed image of (a). Green lines show the LC nematic director orientation reconstructed from the bacterial orientation. Several defects are present. (c) Bacterial concentration distribution in the area indicated by the blue dashed box in (b). Colors represent the concentration of bacteria extracted from the averaged fluorescence intensity. Two topological defects ($1/2$ and $-1/2$) are highlighted. White lines show defect orientations. Scale bar is 50 μm. (d) Bacterial concentration profiles around the defects. Blue line represents a concentration profile in the vicinity of $1/2$ defect along the white dashed line in (d). $x = 0$ corresponds to the center of $1/2$ defect. The red line represents a concentration profile in the vicinity of $-1/2$ defect. Concentration profiles along three white dashed lines are averaged. Inset: Bacterial concentration profiles along the lines passing through the cores of defects extracted from the computational model for $c_0 = 0.3$, $\tau = 66.6$ and corresponding to Fig. 4(c).

integration and averaged over the duration of the run. The inset of Fig. 4(a) shows $\Delta c/c_0$ vs the average defect speed inferred from Fig. 3(b). One sees that the accumulation vanishes in the limit of very high defect speeds. In this case, the dynamics is characterized by frequent creation and annihilation of $\pm 1/2$ defect pairs. Since nearby $\pm 1/2$ defects produce an opposite trend on the concentration, the overall effect is smeared out. In addition, rapidly moving defects accumulate fewer bacteria. Figure 4(b) confirms that the accumulation or depletion vanishes with the decrease in the bacteria reversal time τ.

C. Experimental verification

We perform experiments with swimming bacteria *B. subtilis* suspended in a freestanding film of lyotropic liquid crystal disodium cromoglycate (DSCG) [32]. Previous experiments with bacteria suspended in liquid crystals were performed either in thin closed glass cells or in pendant drops [32–36]. The freestanding geometry was necessary to minimize the effect of in-plane surface anchoring. The experimental setup is similar to that used in our previous works [5,12]. A small drop (7 μL) of a bacterial suspension in LC is placed between four thin movable fibers and then stretched to produce a thin freestanding liquid film.

To increase the accuracy of bacteria recognition and the overall data fidelity, we use a fluorescent DK400 strain of *B. subtilis*; see Video 5 in Supplemental Material [39]. The local concentration of bacteria and the nematic director orientation are extracted from the fluorescent images by a custom MATLAB script; see the Appendix. The main experimental results are shown in Fig. 5. The need for fluorescent bacteria is twofold. Firstly, we determine the

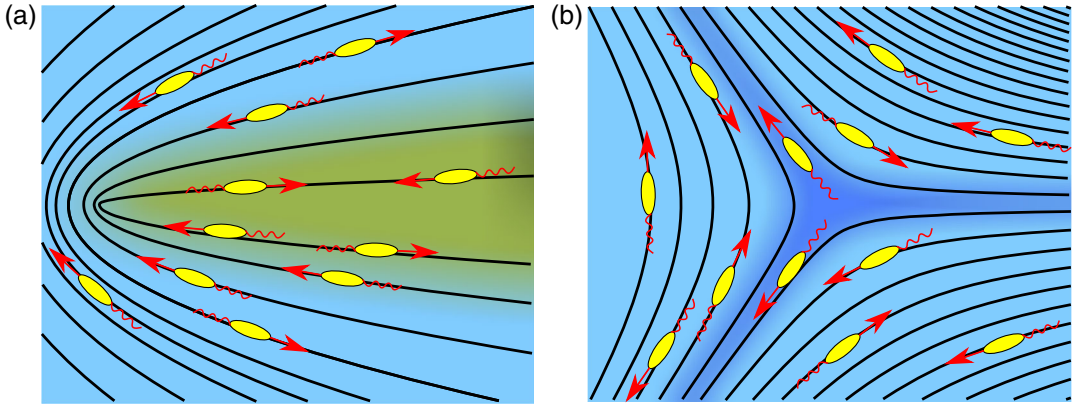

FIG. 6. Illustration of accumulation and depletion of bacteria in topological defects. (a) Accumulation of bacteria in $+1/2$ defect. Bacteria accumulate in the yellow region due to the convergence of bacterial trajectories. (b) Bacteria escape from the dark blue region of $-1/2$ defect independently of their initial orientation.

bacterial local concentration from the fluorescence intensity. Secondly, from the orientation of bacteria, we reconstruct the local director field. A conventional bright field microscopy does not allow direct measurement of the concentration and orientation of bacteria around LC defects due to birefringence-induced optical distortions of the images. Brightness variations of the transmitted light are caused both by the presence of bacteria and by steep fluctuations of the LC orientation.

At a relatively high bacterial concentration $c \approx 6 \times 10^9$ cell/cm^3 (or about 2% volume fraction), we observe a large number of rapidly moving defects; see Videos 6 and 7 in Supplemental Material [39]. Large defect speeds and strong shape fluctuations do not allow bacterial accumulation or depletion in the defect locations. However, at lower concentration $c \approx 2 \times 10^9$ cell/cm^3, the mean defect speed is significantly smaller, in faithful agreement with our theoretical predictions; see Videos 8 and 9 in Supplemental Material [39]. Slowly moving and more persistent defects lead to a substantial accumulation of bacteria in $1/2$ defects and expulsion from the cores of $-1/2$ defects; see Figs. 5(a), 5(b), and 5(d). The magnitude of bacterial concentration fluctuations at lower c values may reach 30%–50%. The coarse-grained experimental concentration distributions around the defects have a similar trend with the prediction of the computational model; compare Fig. 5(c) and Fig. 4(c). Moreover, the concentration profiles along the lines passing through defect cores, Fig. 5(c), show qualitatively similar behavior with the computational model; see inset of Fig. 5(d).

While we clearly see a decrease in the trapped bacteria number with the defect speed, it is hard to make a more quantitative statement because the defect speed cannot be controlled directly: it itself depends on the concentration of bacteria. Moreover, an increase in the bacterial concentration makes the dynamics more turbulent and, in turn, leads to the overall increase in the number of defects. These issues can be possibly addressed in a new generation of experiments where moving defects can be created by surface patterning and their speed can be controlled by the concentration of oxygen available to bacteria.

IV. DISCUSSION

A. Heuristic explanation of the accumulation and depletion phenomena

The accumulation and depletion are directly related to the nematic director topology at the defect cores. Consider, for simplicity, nonreversing bacteria, $\tau \gg 1$. Since the nematic streamlines, and, respectively, the bacterial trajectories, converge at the core of the $+1/2$ defect, bacteria swimming towards the defect accumulate in the core, Fig. 6(a). At the same time, bacteria swimming in the opposite direction will leave the defect. This will lead to the overall increase in the concentration. The accumulation domain is highlighted in Fig. 6(a). In contrast, the $-1/2$ defect creates a nematic configuration that expels the bacteria independently of their orientation, Fig 6(b). Bacteria close to the defect core (in the dark blue region) swim away. However, bacteria swimming towards the defect are deflected and cannot influence the bacterial concentration near the core. Accumulation or depletion attenuates with the reversal time τ decrease, in agreement with our numerical analysis; see Fig. 4(b). A more quantitative explanation of these phenomena in terms of the concentration fluxes is presented in the following section.

B. Stability of the aligned state

We examine linear stability of the homogeneous aligned state $c^+ = c^- = c_0/2$, $\mathbf{n} = (1, 0)$; see Supplemental Material [39]. The growth rates $\sigma(\mathbf{k})$ of small perturbations

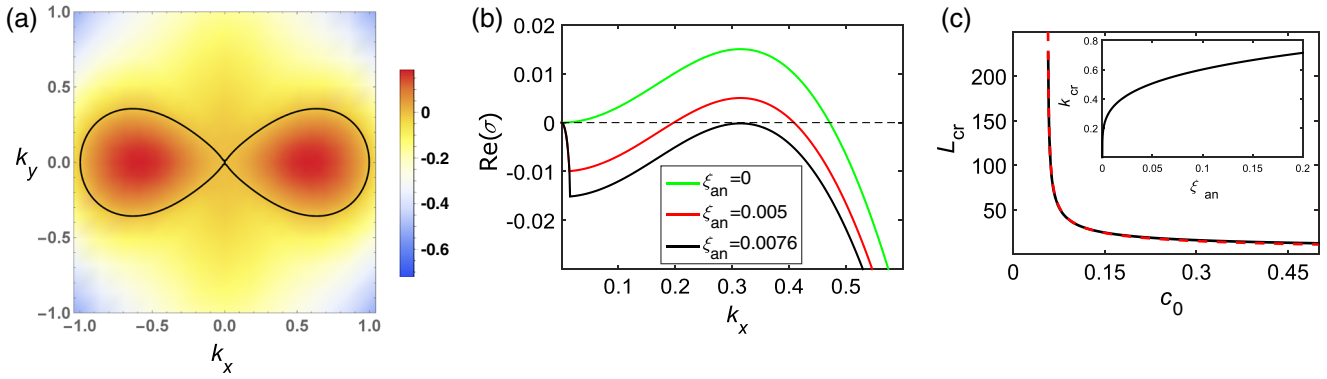

FIG. 7. Linear stability analysis of the aligned state. (a) Density plot of the growth rate $\mathrm{Re}[\sigma(\mathbf{k})]$ vs k_x, k_y for $\xi_{\mathrm{an}} = 0$. Maximum growth rate occurs along the nematic direction (x axis). (b) $\mathrm{Re}[\sigma(\mathbf{k})]$ vs k_x, $k_y = 0$, for different ξ_{an} values, $c_0 = 0.2$. (c) Critical wavelength $L_{\mathrm{cr}} = 2\pi/k_{\mathrm{cr}}$ vs c, from Eq. (8). The dashed line is the fit $L_{\mathrm{cr}} \sim 1/\sqrt{c - c_{\mathrm{cr}}}$. Inset: k_{cr} vs ξ_{an}, from Eq. (10).

vs the wave number $\mathbf{k}$ are shown in Fig. 7(a). In qualitative agreement with experiment [32], the instability initially occurs for the perturbations with the wave vector parallel to the nematic direction, i.e., for the longitudinal undulations. For zero anchoring, the most unstable wave number k_{cr} is given by the following analytic expression (see Supplemental Material [39]),

$$k_{\mathrm{cr}} = \frac{1}{h}\sqrt{\sqrt{\frac{12(\xi+1)[(12(\xi+1)+h^2\mathrm{Er}c_0\Lambda]}{2\Gamma+(\xi+1)^2}} - 12}, \quad (8)$$

where $\mathrm{Er} = \eta V_0 l/K$ is the Ericksen number (i.e., the ratio of viscous stress to elastic stress), l is the bacterium length, and K is the average elastic constant. For the conditions of the experiment [32], the Ericksen number is $\mathrm{Er} \approx 3.75$. $\xi \approx 1$ is the aspect ratio parameter in the Edwards-Beris theory. Without anchoring, the instability is long wavelength, with zero critical wave number at the threshold. With the increase in c, the critical wave number increases. However, the instability becomes short wavelength with a finite critical wave number k_{cr} for a nonzero anchoring; see Fig. 7(b).

The critical concentration c_{cr} for the onset of undulation instability is given by (see Supplemental Material [39])

$$c_{\mathrm{cr}} = 4\frac{\mathrm{Er}\xi_{\mathrm{an}}h^2 + \sqrt{12h^2\mathrm{Er}\xi_{\mathrm{an}}[2\Gamma+(\xi+1)^2]} + 6\Gamma}{h^2\mathrm{Er}(\xi+1)\Lambda}. \quad (9)$$

Correspondingly, the critical wave number k_{cr} at the threshold ($c = c_{\mathrm{cr}}$) as a function of anchoring is of the form

$$k_{\mathrm{cr}} = 2\left(\frac{3\mathrm{Er}\xi_{\mathrm{an}}}{h^2[2\Gamma+(\xi+1)^2]}\right)^{1/4}. \quad (10)$$

As one sees from Eq. (9), the critical concentration decreases with the increase in the dipole strength Λ; see Eq. (3). Also, c_{cr} increases with the decrease in the cell thickness h and increase in the anchoring strength ξ_{an}. We find that the most unstable wavelength scales roughly as $1/\sqrt{c - c_{\mathrm{cr}}}$, again in a good agreement with Ref. [32], Fig. 7(c). At the threshold, the critical wave number k_{cr} increases with the anchoring strength as $k_{\mathrm{cr}} \sim \xi_{\mathrm{an}}^{1/4}$; see inset of Fig. 7(c).

C. Concentration distributions for moving defects

We investigate the concentration distributions generated by moving isolated defects. We assume that the director orientations for $\pm 1/2$ defects are close to the stationary ones, i.e., $\theta = \pm(\varphi + \pi)/2$, where φ is the polar angle with respect to the x axis. We seek a steady-state solution to Eq. (7) for the defects moving with speed V, i.e., $c(x - Vt)$, $w(x - Vt)$. In the comoving frame, Eq. (7) assumes the form

$$\begin{aligned} -V\partial_x c + \nabla\cdot(V_0\mathbf{n}_0 w) &= D_c\nabla^2 c, \\ -V\partial_x w + \nabla\cdot(V_0\mathbf{n}_0 c) &= -\frac{2w}{\tau} + D_c\nabla^2 w, \end{aligned} \quad (11)$$

where $\mathbf{n}_0 = [\pm\sin(\theta), \cos(\theta)]$ for $\pm 1/2$ defects, correspondingly. For simplicity, we neglect the advection terms $\sim\mathbf{v}$. Coupled elliptic equations (11) are solved numerically on a rectangular domain with appropriate boundary conditions. Because of reflection symmetry along the x axis, the equations may be solved only for $y > 0$. Correspondingly, the Neumann boundary conditions $\partial_y c(x, y) = \partial_y w = 0$ are imposed for $y = 0$. A condition $w(x, 0) = 0$ for $x > 0$ is imposed along the branch cut of θ. Far from the defect, for $y = L_0 \gg 1$, the Dirichlet condition $c(x, L_0) = c_0$, $w(x, L_0) = 0$ is imposed. Result are shown in Figs. 4(d) and 4(e). We see that there is an accumulation of bacteria slightly behind the $1/2$ defects and expulsion from the $-1/2$ defects, similar to that obtained by the solution of the full system, Fig. 4(c). Distributions of the concentration difference w for both cases are shown in Fig. 4 of the Supplemental Material (see also Supplemental

Material for details) [39]. An exact threefold symmetry is expected for a stationary $-1/2$ defect in an infinite domain. Here, the threefold symmetry is broken due to the defect motion ($V \neq 0$) and by a finite size of the integration domain.

The magnitude of $\Delta c/c_0$ decreases with the increase of the defect speed V. We find that the decay of $\Delta c/c_0$ versus defect speed V in the full model is faster than that in the reduced model, Eq. (11). In the full model, the increase in the defect speed V is due to concentration increase. That results in an increase in the defect number. These defects move chaotically and are created or annihilated in pairs. This nonstationary defect dynamics, effectively reducing the accumulation of bacteria in the cores, is not captured by the simplified model.

We find that $\Delta c \to 0$ for $\tau \to 0$. In the limit $\tau \to 0$ and $V = 0$, one obtains analytic solutions for the concentration distributions:

$$c_{1/2} \approx c_0 + \frac{\tau V_0^2 c_0}{8D_c}\cos\varphi, \qquad c_{-1/2} \approx c_0 - \frac{\tau V_0^2 c_0}{24D_c}\cos 3\varphi. \tag{12}$$

For $\tau \to 0$, Eq. (7) is reduced to the active nematic model [27–30]. In this limit there is no accumulation or depletion of bacteria in the cores of topological defects; see Fig. 4(b).

V. CONCLUSIONS

We develop a computational model describing the biosynthetic system of motile bacteria suspended in lyotropic liquid crystals. The most crucial difference from the phenomenological models of active nematics [27–31] is that we explicitly introduce two populations of bacteria, c^+, c^-, traveling in opposite directions. The interaction between the populations is due to random reorientations characterized by the reversal time τ. This description is truly needed to capture the experimentally observed behavior—in liquid crystals, bacteria swim on opposite tracks almost without interactions. We also demonstrate that previous models, Refs. [27–31], could be rigorously derived from our system in the limit of $\tau \to 0$. However, for the conditions of our experiment this limit is unphysical. Another important difference is that we consider the effect of surface anchoring, which to the best of our knowledge was not studied before in the context of active matter. Surface anchoring is of crucial importance for the living liquid crystals. The above differences lead to a wealth of new phenomena. Firstly, accumulation and depletion phenomena are not present in Refs. [27–31]. Secondly, we obtain finite wave number instability and a hysteretic transition between the homogeneously aligned state and the chaotic states with topological defects.

Our computational model is in a good agreement with the experiment and yields testable predictions. Some of these predictions are readily confirmed by our experiment with a freestanding bacterial film. The model can be extended in many directions. For example, the anisotropy of the elastic constants and viscosities can be readily incorporated. While we do not anticipate qualitative changes in the behavior, this generalization may have an effect on the interaction of defects; e.g., it can significantly increase the defect annihilation time.

Topological defects often play a role of elementary excitations that control the surrounding dynamics in active systems [18,27,48]. Accumulation and depletion of bacteria in the cores of topological defects significantly changes the defect dynamics (since the activity and, correspondingly, the defect velocity are proportional to the bacterial concentration). Thus, it provides a nontrivial feedback between topology and activity.

Our discovery of accumulation of bacteria in the cores of $1/2$ topological defects may have intriguing implications. The related phenomenon also occurs in other active systems, e.g., in tissue formed by cultured stem cells [49]. Topological defects in liquid crystals form whenever the system is confined, even in equilibrium, thanks to the surface anchoring of the director and nontrivial Euler characteristic of any closed surface (except a torus). Furthermore, these defects can be guided by applied electric or magnetic fields, surface anchoring, light, or chemical and temperature gradients. These findings extend our scope of tools to control and manipulate microscopic objects in active matter [33,36,50,51]. Moreover, with the recent progress in the lithographic design of light-sensitive surface anchoring patterns, topological defects can be created on demand and guided by light [52]. Thus, our findings open a possibility to precisely manipulate a few bacteria or imprint the desired pattern of bacterial concentration. This effect can be used in a variety of applications for express identification or recognition of bacteria and in the development of bacteria-powered micromachines [53–55]. We anticipate that the number of trapped bacteria will fluctuate in a wide range in the turbulent regime. However, in a laminar regime, the number of bacteria will be preserved and can be tuned by the defect speed.

Recent experiments [56] on dilute suspensions of bacteria in patterned chromonic liquid crystals with preimposed director field show that *B. subtilis* can distinguish between defects of different topological charge and of different geometry. In particular, bacteria can accumulate at the cores of radial defects of strength $+1$, form unidirectionally rotating vortices around defects of strength $+1$ with a spiraling director of a bend-splay type, and avoid defects of strength -1. Furthermore, the bacteria prefer to move away from the $-1/2$ defects towards the $1/2$ defects [56]. One should, however, bear in mind that the experimental setting of Ref. [56] with immobilized (and engraved) topological defects and low concentrations of bacteria is principally different from the experimental

conditions discussed in this work, in which the defects of strength $1/2$ and $-1/2$ nucleate as a result of bacterial activity in concentrated suspensions and constantly move thanks to the shear flows produced by the bacteria. The experimental results presented in Ref. [56] and in this work thus complement each other and demonstrate that the prevalence of active swimmers at the cores of $1/2$ defects and their depletion near $-1/2$ defects is a universal phenomenon observed both below and above the threshold of topological turbulence.

ACKNOWLEDGMENTS

We thank Professor Daniel Kearns for providing the fluorescent strains of *Bacillus subtilis*. M. M. G., A. S., and I. S. A. were supported by the U.S. Department of Energy, Office of Basic Energy Sciences, Division of Materials Science and Engineering. O. D. L. was supported by NSF Grant No. DMR-1507637.

APPENDIX: MATERIALS AND METHODS

1. Edwards-Beris equations for the liquid crystal evolution

The tensor $\mathbf{S}$ in Eq. (1) is of the form (see Supplemental Material [39])

$$\mathbf{S} = (\xi\mathbf{A} + \mathbf{\Omega})\left(\mathbf{Q} + \frac{\mathbf{I}}{2}\right) + \left(\mathbf{Q} + \frac{\mathbf{I}}{2}\right)(\xi\mathbf{A} + \mathbf{\Omega}) - \xi(2\mathbf{Q} + \mathbf{I})\mathrm{Tr}(\mathbf{QW}),$$

where $\xi \approx 1$ is the aspect ratio parameter. The rate of strain and vorticity tensors $\mathbf{A}$, $\mathbf{\Omega}$ are correspondingly symmetric and antisymmetric parts of the velocity gradient tensor $W_{ij} = \partial_i v_j$. The molecular field tensor $\mathbf{H}$ is defined as

$$\mathbf{H} = -\frac{\delta F}{\delta \mathbf{Q}} + \frac{\mathbf{I}}{2}\mathrm{Tr}\left(\frac{\delta F}{\delta \mathbf{Q}}\right),$$

where F is the elastic free energy. Since we are considering a two-dimensional case, there are only two elastic constants K_1 (bend) and K_3 (splay). We assume for simplicity $K_1 = K_3 = K$. The free energy F is written in the Landau–de Gennes form

$$F = \int d\mathbf{r}\left[-\frac{a}{2}Q_{\alpha\beta}Q_{\beta\alpha} + \frac{b}{4}(Q_{\alpha\beta}Q_{\beta\alpha})^2 + \frac{K}{2}(\partial_\gamma Q_{\alpha\beta})^2\right],$$

where a, b are the coefficients from Landau–de Gennes expansion. The symmetric tensor $\boldsymbol{\sigma}_s$ in Eq. (2) is of the form

$$\boldsymbol{\sigma}_s = -\xi\mathbf{H}\left(\mathbf{Q} + \frac{\mathbf{I}}{2}\right) - \xi\left(\mathbf{Q} + \frac{\mathbf{I}}{2}\right)\mathbf{H} + \xi(2\mathbf{Q} + \mathbf{I})\mathrm{Tr}(\mathbf{QH}) - \nabla\mathbf{Q}\colon \frac{\delta F}{\delta \nabla \mathbf{Q}}.$$

Here, $\boldsymbol{\sigma}_a = \mathbf{QH} - \mathbf{HQ}$ is antisymmetric tensor and $\boldsymbol{\sigma}_{\mathrm{visc}} = 2\eta\mathbf{A}$ is viscous tensor. The often used form of the tensor $\mathbf{F}_{\mathrm{exter}}$ is [26] $\mathbf{F}_{\mathrm{exter}} = \xi_{\mathrm{an}}(\mathbf{ff} - \mathbf{I}/2)$, where $\mathbf{f}$ is a unit vector along the aligning field direction (e.g., magnetic field) and ξ_{an} is the alignment strength. The effect of surface anchoring can be modeled in 2D as an aligning field. However, this representation of the external field effect also alters the order parameter magnitude $|\mathbf{Q}|$. We use instead an alternative version of the aligning term that changes only the orientation of the nematic but does not change its amplitude:

$$\mathbf{F}_{\mathrm{exter}} = 4\xi_{\mathrm{an}}\mathbf{Q}\mathbf{R}_{\pi/2}\mathrm{Tr}[\mathbf{Q}(\mathbf{ff} - \mathbf{I}/2)\mathbf{R}_{\pi/2}],$$

where $\mathbf{R}_{\pi/2}$ is the tensor of rotation by $\pi/2$. These two representations yields the same aligning term in the corresponding Ericksen-Leslie equations [25] derived from the Edwards-Beris model [26].

2. Numerical implementation

Equations (1), (2), and (7) are integrated in a double-periodic domain by a semi-implicit fast Fourier transformation method. The algorithm is implemented on the graphical processing units. A typical number of mesh points is 1024×1024. Runs with 2048×2048 points are performed for verification of finite-size effects. Details of the numerical implementation can be found in Supplemental Material [39]. The main model parameters are summarized in Table I. Numerical solution of Eqs. (1), (2), and (7) reveal a number of nontrivial artifacts related to the mapping of a vector field for the bacterial orientation to the nematic director. Firstly, directions $\pm\pi/2$ are identical for the nematic. Since for $\theta = \pm\pi/2$ the distinctions between the fields $c^{\pm}$ is formally lost, it results in a nonphysical collision of bacteria in the $c^{\pm}$ fields. The collisions are manifested by linear δ functions in equations for $c^{\pm}$ along the lines where θ changes from $-\pi/2$ to $\pi/2$ (branch cuts); see Fig. 1 in Supplemental Material [39]. In order to eliminate this artifact, we track the branch cuts and relabel the fields $c^{\pm}$; see Fig. 2 in Supplemental Material [39]. Second artifact is associated with the director indeterminacy at the core of topological defects that invalidates the assumption that bacteria swim along the director. In order to remove this artifact, we decrease the reversal time τ near defect cores. It allows the bacteria to reverse the direction and avoid trapping in the cores. The defect tracking algorithm is described in Supplemental Material and Fig. 3 of the Supplemental Material [39].

3. Scaling of model parameters

The coordinates x, y are normalized by the bacterial length $l = 5$ μm. Velocities are normalized by the bacterial velocity $V_0 = 15$ μm/ sec. Time is normalized by l/V_0. Concentrations are normalized by l^{-3}. Viscosities are

TABLE I. Model parameters.

Parameter	Value	Description
		Parameters of LC
K	10–15	Elastic constant (pN)
Er	3.75	Ericksen number
Γ	1	Relaxation rate (msec/kg)
η	0.5	Isotropic viscosity (kg/msec)
ξ_{an}	0–0.6	Anchoring strength (1/ sec)
h	20–30	Thickness (μm)
ξ	0.9	Aspect ratio parameter
a	0.4	Landau–de Gennes coefficient (N/m^2)
b	0.8	Landau–de Gennes coefficient (N/m^2)
		Parameters for bacterial transport
l	5	Bacterial length (μm)
V_0	15	Bacterial speed (μm/ sec)
τ	50–100	Reversal time (sec)
D_c	200–300	Concentration diffusion (μm^2/ sec)
Λ	187.5	Dipolar strength (pNμm)

normalized by $\eta = 0.5$ kg/m sec. Landau–de Gennes coefficients a and b are normalized by K/l^2, where $K = 10$ pN is the average elasticity constant. Correspondingly, the diffusion coefficient D_c is normalized by lV_0, the viscous friction coefficient ζ by η/l^2, the dipole strength Λ is scaled by $\eta l^2 V_0$, Γ by $1/\eta$, and the anchoring strength ξ_{an} is normalized by U_0/l. The Ericksen number is $\mathrm{Er} = \eta l V_0/K = 3.75$.

4. Experimental details

Bacteria growth.—Experiments are conducted with the *B. subtilis* fluorescent strain DK400 [57]. The bacteria are initially grown on the lysogeny broth (LB) agar plates, then transferred to the LB liquid medium and grown in a shaking incubator at the temperature 35 °C for 10–12 h. The bacteria are extracted from the growth medium by centrifugation at the end of their exponential growth stage and washed. Then the bacteria are suspended in the liquid crystal to achieve the final bacteria concentration of about $(2–6) \times 10^9$ cell/cm^3 and a final concentration of the DSCG mesogenic material at 14 wt%.

Liquid crystal preparation.—Chromonic lyotropic LC DSCG purchased from Spectrum Chemicals, 98% purity, is dissolved in the LB (L3022 SIGMA) at 20 wt%. This solution is added to the concentrated bacteria obtained by the protocol described above. The experiments are started immediately after a drop of bacteria and LC is suspended and stretched between four fibers. The experimental cell is enclosed in an optically transparent box with a controlled humidity level and temperature. We maintain the humidity level close to 100% to minimize evaporation of water and to keep the temperature around 30 °C. Evaporation of even a small fraction of water from the surface of the film leads to a noticeable increase of the viscosity in a very thin surface layer. That effectively introduces a no-slip condition for the fluid flow at the film surface.

Microscopy data acquisition and analysis.—An inverted microscope Olympus IX71 with a motorized stage mounted on a piezoelectric isolation platform Herzan TS-150 and a monochrome Prosilica GX 1660 camera (resolution of 1600×1200) are used to record the fluorescent images with the frame rate of 10 fps, at 10× magnification. The acquired images are processed in MATLAB. Local bacterial concentration is assumed to be proportional to the average fluorescent brightness of a considered area. The fluorescent intensity of the areas with no bacteria and fluorescent intensity averaged over the entire image are used for the concentration calibration. The nematic director orientation of LC is reconstructed from the local orientation of bacteria with a custom MATLAB script. The local orientation of the bacteria is estimated as a line along the bacteria edges, detected by calculating a gradient of the fluorescent intensity of each pixel of the image.

[1] S. Ramaswamy, *The Mechanics and Statistics of Active Matter*, Annu. Rev. Condens. Matter Phys. **1**, 323 (2010).

[2] A. Cavagna, A. Cimarelli, I. Giardina, G. Parisi, R. Santagati, F. Stefanini, and M. Viale, *Scale-Free Correlations in Starling Flocks*, Proc. Natl. Acad. Sci. U.S.A. **107**, 11865 (2010).

[3] I. D. Couzin, J. Krause, R. James, G. D. Ruxton, and N. R. Franks, *Collective Memory and Spatial Sorting in Animal Groups*, J. Theor. Biol. **218**, 1 (2002).

[4] C. Dombrowski, L. Cisneros, S. Chatkaew, R. E. Goldstein, and J. O. Kessler, *Self-Concentration and Large-Scale Coherence in Bacterial Dynamics*, Phys. Rev. Lett. **93**, 098103 (2004).

[5] A. Sokolov, I. S. Aranson, J. O. Kessler, and R. E. Goldstein, *Concentration Dependence of the Collective Dynamics of Swimming Bacteria*, Phys. Rev. Lett. **98**, 158102 (2007).

[6] T. Surrey, F. Nédélec, S. Leibler, and E. Karsenti, *Physical Properties Determining Self-Organization of Motors and Microtubules*, Science **292**, 1167 (2001).

[7] V. Schaller, C. Weber, C. Semmrich, E. Frey, and A. R. Bausch, *Polar Patterns of Driven Filaments*, Nature (London) **467**, 73 (2010).

[8] Y. Sumino, K. H. Nagai, Y. Shitaka, D. Tanaka, K. Yoshikawa, H. Chaté, and K. Oiwa, *Large-Scale Vortex Lattice Emerging from Collectively Moving Microtubules*, Nature (London) **483**, 448 (2012).

[9] J. Palacci, S. Sacanna, A. P. Steinberg, D. J. Pine, and P. M. Chaikin, *Living Crystals of Light-Activated Colloidal Surfers*, Science **339**, 936 (2013).

[10] I. Theurkauff, C. Cottin-Bizonne, J. Palacci, C. Ybert, and L. Bocquet, *Dynamic Clustering in Active Colloidal Suspensions with Chemical Signaling*, Phys. Rev. Lett. **108**, 268303 (2012).

[11] H. H. Wensink, J. Dunkel, S. Heidenreich, K. Drescher, R. E. Goldstein, H. Löwen, and J. M. Yeomans, *Meso-Scale*

Turbulence in Living Fluids, Proc. Natl. Acad. Sci. U.S.A. **109**, 14308 (2012).

[12] A. Sokolov and I. S. Aranson, *Physical Properties of Collective Motion in Suspensions of Bacteria*, Phys. Rev. Lett. **109**, 248109 (2012).

[13] D. Saintillan and M. J. Shelley, *Instabilities and Pattern Formation in Active Particle Suspensions: Kinetic Theory and Continuum Simulations*, Phys. Rev. Lett. **100**, 178103 (2008).

[14] I. S. Aranson, A. Sokolov, J. O. Kessler, and R. E. Goldstein, *Model for Dynamical Coherence in Thin Films of Self-Propelled Microorganisms*, Phys. Rev. E **75**, 040901 (2007).

[15] A. Sokolov and I. S. Aranson, *Reduction of Viscosity in Suspension of Swimming Bacteria*, Phys. Rev. Lett. **103**, 148101 (2009).

[16] H. M. López, J. Gachelin, C. Douarche, H. Auradou, and E. Clément, *Turning Bacteria Suspensions into Superfluids*, Phys. Rev. Lett. **115**, 028301 (2015).

[17] T. Sanchez, D. T. N. Chen, S. J. DeCamp, M. Heymann, and Z. Dogic, *Spontaneous Motion in Hierarchically Assembled Active Matter*, Nature (London) **491**, 431 (2012).

[18] F. C. Keber, E. Loiseau, T. Sanchez, S. J. DeCamp, L. Giomi, M. J. Bowick, M. C. Marchetti, Z. Dogic, and A. R. Bausch, *Topology and Dynamics of Active Nematic Vesicles*, Science **345**, 1135 (2014).

[19] S. J. DeCamp, G. S. Redner, A. Baskaran, M. F. Hagan, and Z. Dogic, *Orientational Order of Motile Defects in Active Nematics*, Nat. Mater. **14**, 1110 (2015).

[20] T. Gao, R. Blackwell, M. A. Glaser, M. D. Betterton, and M. J. Shelley, *Multiscale Modeling and Simulation of Microtubule–Motor-Protein Assemblies*, Phys. Rev. E **92**, 062709 (2015).

[21] S. Ramaswamy, R. A. Simha, and J. Toner, *Active Nematics on a Substrate: Giant Number Fluctuations and Long-Time Tails*, Europhys. Lett. **62**, 196 (2003).

[22] A. Baskaran and M. C. Marchetti, *Hydrodynamics of Self-Propelled Hard Rods*, Phys. Rev. E **77**, 011920 (2008).

[23] E. Bertin, H. Chaté, F. Ginelli, S. Mishra, A. Peshkov, and S. Ramaswamy, *Mesoscopic Theory for Fluctuating Active Nematics*, New J. Phys. **15**, 085032 (2013).

[24] S. Ngo, A. Peshkov, I. S. Aranson, E. Bertin, F. Ginelli, and H. Chaté, *Large-Scale Chaos and Fluctuations in Active Nematics*, Phys. Rev. Lett. **113**, 038302 (2014).

[25] M. Kleman and O. D. Lavrentovich, *Soft Matter Physics: An Introduction* (Springer Science & Business Media, New York, 2007).

[26] A. N. Beris and B. J. Edwards, *Thermodynamics of Flowing Systems: With Internal Microstructure*, Oxford Engineering Science Series (Oxford University Press, New York, 1994), Vol. 36.

[27] L. Giomi, M. J. Bowick, X. Ma, and M. C. Marchetti, *Defect Annihilation and Proliferation in Active Nematics*, Phys. Rev. Lett. **110**, 228101 (2013).

[28] S. P. Thampi, R. Golestanian, and J. M. Yeomans, *Velocity Correlations in an Active Nematic*, Phys. Rev. Lett. **111**, 118101 (2013).

[29] S. P. Thampi, R. Golestanian, and J. M. Yeomans, *Active Nematic Materials with Substrate Friction*, Phys. Rev. E **90**, 062307 (2014).

[30] M. L. Blow, S. P. Thampi, and J. M. Yeomans, *Biphasic, Lyotropic, Active Nematics*, Phys. Rev. Lett. **113**, 248303 (2014).

[31] L. Giomi, *Geometry, and Topology of Turbulence in Active Nematics*, Phys. Rev. X **5**, 031003 (2015).

[32] S. Zhou, A. Sokolov, O. D. Lavrentovich, and I. S. Aranson, *Living Liquid Crystals*, Proc. Natl. Acad. Sci. U.S.A. **111**, 1265 (2014).

[33] A. Sokolov, S. Zhou, O. D. Lavrentovich, and I. S. Aranson, *Individual Behavior and Pairwise Interactions between Microswimmers in Anisotropic Liquid*, Phys. Rev. E **91**, 013009 (2015).

[34] A. Kumar, T. Galstian, S. K. Pattanayek, and S. Rainville, *The Motility of Bacteria in an Anisotropic Liquid Environment*, Mol. Cryst. Liq. Cryst. **574**, 33 (2013).

[35] P. C. Mushenheim, R. R. Trivedi, H. H. Tuson, D. B. Weibel, and N. L. Abbott, *Dynamic Self-Assembly of Motile Bacteria in Liquid Crystals*, Soft Matter **10**, 88 (2014).

[36] P. C. Mushenheim, R. R. Trivedi, S. S. Roy, M. S. Arnold, D. B. Weibel, and N. L. Abbott, *Effects of Confinement, Surface-Induced Orientations and Strain on Dynamical Behaviors of Bacteria in Thin Liquid Crystalline Films*, Soft Matter **11**, 6821 (2015).

[37] M. Tasinkevych, F. Mondiot, O. Mondain-Monval, and J.-C. Loudet, *Dispersions of Ellipsoidal Particles in a Nematic Liquid Crystal*, Soft Matter **10**, 2047 (2014).

[38] C. W. Harvey, M. Alber, L. S. Tsimring, and I. S. Aranson, *Continuum Modeling of Myxobacteria Clustering*, New J. Phys. **15**, 035029 (2013).

[39] See Supplemental Material at http://link.aps.org/supplemental/10.1103/PhysRevX.7.011029 for details about the 4 supplementary figures, description of the model, numerical methods, defect detection and tracking algorithm, stability analysis, legends to supplementary movies.

[40] S. Kim and S. J. Karrila, *Microhydrodynamics: Principles and Selected Applications* (Courier Corp., New York, 2013).

[41] M. S. Krieger, S. E. Spagnolie, and T. Powers, *Microscale Locomotion in a Nematic Liquid Crystal*, Soft Matter **11**, 9115 (2015).

[42] C. J. Smith and C. Denniston, *Elastic Response of a Nematic Liquid Crystal to an Immersed Nanowire*, J. Appl. Phys. **101**, 014305 (2007).

[43] M. M. Tirado and J. G. de la Torre, *Rotational Dynamics of Rigid, Symmetric Top Macromolecules. Application to Circular Cylinders*, J. Chem. Phys. **73**, 1986 (1980).

[44] Sh. Zhou, K. Neupane, Y. A. Nastishin, A. R. Baldwin, S. V. Shiyanovskii, O. D. Lavrentovich, and S. Sprunt, *Elasticity, Viscosity, and Orientational Fluctuations of a Lyotropic Chromonic Nematic Liquid Crystal Disodium Cromoglycate*, Soft Matter **10**, 6571 (2014).

[45] X.-q. Shi, H. Chaté, and Y.-q. Ma, *Instabilities and Chaos in a Kinetic Equation for Active Nematics*, New J. Phys. **16**, 035003 (2014).

[46] L. M. Pismen, *Dynamics of Defects in an Active Nematic Layer*, Phys. Rev. E **88**, 050502 (2013).

[47] K. Kohlstedt, A. Snezhko, M. V. Sapozhnikov, I. S. Aranson, J. S. Olafsen, and E. Ben-Naim, *Velocity Distributions of Granular Gases with Drag and with Long-Range Interactions*, Phys. Rev. Lett. **95**, 068001 (2005).

[48] I. S. Aranson and L. Kramer, *The World of the Complex Ginzburg-Landau Equation*, Rev. Mod. Phys. **74**, 99 (2002).

[49] K. Kawaguchi, R. Kageyama, and M. Sano, *Topological Defect Launches 3D Mound in the Active Nematic Sheet of Neural Progenitors*, arXiv:1605.06470.

[50] A. Sokolov and I. S. Aranson, *Rapid Expulsion of Microswimmers by a Vortical Flow*, Nat. Commun. **7**, 11114 (2016).

[51] P. Guillamat, J. Ignés-Mullol, and F. Sagués, *Control of Active Liquid Crystals with a Magnetic Field*, Proc. Natl. Acad. Sci. U.S.A. **113**, 5498 (2016).

[52] Y. Guo, M. Jiang, Ch. Peng, K. Sun, O. Yaroshchuk, O. Lavrentovich, and Q.-H. Wei, *High-Resolution and High-Throughput Plasmonic Photopatterning of Complex Molecular Orientations in Liquid Crystals*, Adv. Mater. **28**, 2353 (2016).

[53] A. Sokolov, M. M. Apodaca, B. A. Grzybowski, and I. S. Aranson, *Swimming Bacteria Power Microscopic Gears*, Proc. Natl. Acad. Sci. U.S.A. **107**, 969 (2010).

[54] R. Di Leonardo, L. Angelani, D. DellArciprete, Giancarlo Ruocco, V. Iebba, S. Schippa, M. P. Conte, F. Mecarini, F. De Angelis, and E. Di Fabrizio, *Bacterial Ratchet Motors*, Proc. Natl. Acad. Sci. U.S.A. **107**, 9541 (2010).

[55] S. P. Thampi, A. Doostmohammadi, T. N. Shendruk, R. Golestanian, and J. M. Yeomans, *Active Micromachines: Microfluidics Powered by Mesoscale Turbulence*, Science Advances **2**, e1501854 (2016).

[56] C. Peng, T. Turiv, Y. Guo, Q. H. Wei, and O. D. Lavrentovich, *Command of Active Matter by Topological Defects and Patterns*, Science **354**, 882 (2016).

[57] K. M. Blair, L. Turner, J. T. Winkelman, H. C. Berg, and D. B. Kearns, *A Molecular Clutch Disables Flagella in the Bacillus Subtilis Biofilm*, Science **320**, 1636 (2008).